Article

Tropical Cyclone Wind Direction Retrieval Based on Wind Streaks and Rain Bands in SAR Images

Zhancai Liu [†], Hongwei Yang [†], Weihua Ai *, Kaijun Ren, Shensen Hu and Li Wang

College of Meteorology and Oceanography, National University of Defense Technology, Changsha 410073, China;
liuzc1842@nudt.edu.cn (Z.L.); yhw19@nudt.edu.cn (H.Y.); renkaijun@nudt.edu.cn (K.R);
hushensen18@nudt.edu.cn (S.H.); warren@whu.edu.cn (L.W.)
* Correspondence: aiweihua@nudt.edu.cn
† These authors contributed equally to this work.

Abstract: Tropical cyclones (TCs) are associated with severe weather phenomena, making accurate wind field retrieval crucial for TC monitoring. SAR's high-resolution imaging capability provides detailed information for TC observation, and wind speed calculations require wind direction as prior information. Therefore, utilizing SAR images to retrieve TC wind fields is of significant importance. This study introduces a novel approach for retrieving wind direction from SAR images of TCs through the classification of TC sub-images. The method utilizes a transfer learning-based Inception V3 model to identify wind streaks (WSs) and rain bands in SAR images under TC conditions. For sub-images containing WSs, the Mexican-hat wavelet transform is applied, while for sub-images containing rain bands, an edge detection technique is used to locate the center of the TC eye and subsequently the tangent to the spiral rain bands is employed to determine the wind direction associated with the rain bands. Wind direction retrieval from 10 SAR TC images showed an RMSD of 19.52° and a correlation coefficient of 0.96 when compared with ECMWF and HRD observation wind directions, demonstrating satisfactory consistency and providing highly accurate TC wind directions. These results confirm the method's potential applications in TC wind direction retrieval.

Keywords: Sentinel-1; SAR images; tropical cyclone (TC); wind direction

1. Introduction

Tropical cyclones (TCs) are intense weather systems capable of causing natural disasters, such as strong winds, heavy rainfall, and storm surges, which significantly impact human safety, lives, and property. In recent years, observation and monitoring of TCs have increased, and Synthetic Aperture Radar (SAR), with its high spatiotemporal resolution, all-weather capability, and ability to penetrate clouds and fog, has become increasingly popular as a means to observe TCs, playing a crucial role [1–3]. Before the landfall of TCs, SAR can provide an early assessment of potential impacts. By analyzing wind fields offshore, we can estimate the maximum sustained winds and the TC's movement, which are critical for forecasting potential land impacts and guiding timely evacuation and preparedness efforts. SAR measures radar backscatter signals from the sea surface by actively emitting electromagnetic waves, thereby generating intensity images of radar backscatter. The roughness of the sea surface, primarily induced by surface tension waves and short gravity waves with wavelengths ranging from a few centimeters to several tens of centimeters, significantly affects the backscatter of the SAR beam. This roughness is influenced by interactions between the sea and the atmosphere, including the effects of unstable boundary layers. In SAR imagery, this is reflected as variations in pixel brightness, which are predominantly caused by wind fields and precipitation over the ocean surface. Unstable atmospheric boundary layers can induce convergence or divergence in the sea surface, altering its roughness and resulting in the formation of linear stripes with a scale

of several kilometers in Synthetic Aperture Radar (SAR) imagery. These stripes, characterized by alternating light and dark bands, are referred to as wind streaks (WSs). In SAR imaging, the modulation of radar backscatter by sea surface wind fields provides a precise characterization of the wind field's inherent properties [4]. Gerling [5], as early as 1986, confirmed that the linear streak features on SeaSat satellite SAR imagery, with scales of the order of several kilometers, are induced by sea surface winds. Later, several scholars have identified a significant correlation between the Normalized Radar Cross-Section (NRCS) and wind vectors, and leveraging this relationship, they have developed several empirical models [6,7]. Moreover, an increasing body of research and observational evidence indicates a strong consistency between sea surface wind direction and directional patterns of WSs observed in SAR imagery [8]. Therefore, one of the methods for extracting wind direction information is to utilize SAR images that contain WSs.

Due to the strong correlation between sea surface wind direction and SAR image features on a large scale [9], and because the co-polarized backscatter signals (VV) are highly sensitive to motion occurring on the ocean surface, the primary method for extracting wind direction from SAR images is to utilize co-polarized backscatter cross-sections. Traditional methods for wind direction retrieval from SAR images mainly include the following approaches: Firstly, the Fast Fourier Transform (FFT) method. Furevik et al. [10] employed FFT to extract wind direction information from SAR images. Additionally, others have also utilized Fourier transform algorithms [11]. Secondly, wavelet analysis is another traditional method for wind direction retrieval. Zhang et al. [12] utilized the Gabor wavelet transform for secondary wavelet decomposition of SAR images, extracting wind direction using the FFT method. Stefano et al. [13] proposed a wind direction extraction method based on two-dimensional continuous wavelet transform (2D-CWT) of SAR images, which was applied for wind field retrieval in coastal areas. Corazza et al. [14] assessed various methods for estimating wave direction from SAR images and proposed an improvement to spectral methods using the Radon transform for wind direction retrieval. Thirdly, the local gradient method (LG). Koch [15] leveraged standard image processing algorithms for LG computation, demonstrating that the LG method accurately determines wind direction under high wind speed conditions. Zhu et al. [16] proposed a method for sea surface wind direction retrieval using LG in SAR images based on digital image processing theory. Upon this foundation, Rana et al. [17] introduced an improved local gradient (LG-Mod) method by substituting directional statistics for histogram analysis results. Xie et al. [18] combined SAR image smoothing with spectral domain LG computation and acquiring LG direction in the spatial domain, and proposed a modified local gradient (ILG-Mod) method, which exhibits superior performance compared to previous local gradient methods. Fan et al. [19] employed the LG method to estimate the wind direction of TCs using dual-polarization (VV + VH) SAR images from the C-band Radersat-2 and Sentinel-1A and the results indicated that dual-polarization SAR is more suitable for TC wind direction estimation compared to single-polarization SAR. The wind direction retrieval algorithms for SAR images mentioned above have been widely applied, yet the retrieval results still exhibit considerable errors. The FFT algorithm achieves an accuracy range of 23–37° with an average root mean square deviation (RMSD) of 28.96°, while the LG algorithm performs within a range of 21–38° with an average RMSD of 32.52° [20]. Moreover, the LG method is susceptible to speckle noise, which introduces errors in the accuracy of wind direction. The wind direction results obtained from the aforementioned methods exhibit a 180° ambiguity issue, necessitating reliance on external data for disambiguation. This represents a crucial challenge, and to date, several methods have been proposed and applied to resolve this ambiguity [21].

However, both the FFT and LG wind direction retrieval methods are limited when SAR images lack WSs [4]. Moreover, the use of VH polarization in radar backscatter reduces sensitivity to radar incidence angles and wind directions, particularly near the eye of TCs. Wang et al. [22] applied an improved LG method (ILG) to extract wind directions from SAR images of TCs, revealing that rain bands could potentially disrupt

gradient directions, thereby reducing the accuracy of retrieved results. Gao et al. [23] extracted rain band streaks from SAR images that do not include the hurricane eye, and proposed a hurricane wind direction retrieval method based on the hurricane inflow angle. Notably, this method does not rely on the hurricane eye or external data. In addition to the aforementioned methods, several new image processing techniques have been shown to have great potential in extracting wind direction information from SAR images. Ni et al. [20] based on the histogram of oriented gradient descriptor and the Hann window function, considered neighboring WSs information, and proposed a new method for extracting TCs wind direction from SAR images using VV and VH signals. Additionally, machine learning methods have been proven to hold significant potential in marine information extraction, particularly in remote sensing image information. Shao et al. [9] utilizing quad-polarization SAR images, discovered that the Polarimetric Coherence Coefficient (PCC) exhibits asymmetric wind direction characteristics in four polarization combinations. They proposed an intelligent method for wind direction retrieval from Gaofen-3 (GF-3) SAR images, combining spectral transformation techniques with machine learning. This method utilized peak intensity spectrum wind direction coefficients, wind direction, azimuth, and slope as inputs. Guo et al. [24] employed deep learning techniques by integrating the Inception V3 convolutional neural network architecture into the recognition of WSs on the ocean surface and achieved wind direction retrieval by identifying SAR sub-images containing WSs using wavelet transformation methods.

Under TC conditions, wind streaks become more pronounced. However, using methods based on WSs to retrieve wind direction in TCs can be compromised by the interference of rain bands, which disrupts the accuracy of the results. Additionally, deep learning-based methods have so far been applied only in non-extreme weather conditions. There are relatively few studies utilizing deep learning tools for wind direction retrieval in TCs. Therefore, leveraging the characteristics of TC imaging in SAR images, such as the lack of wind or rain in the center of TCs in the SAR images and the spiral rain bands surrounding the cyclone center, can enable extraction of wind field information.

This study employs a transfer learning-based Inception V3 neural network to identify WSs and rain bands in SAR imagery under TC conditions. Different methods are applied to retrieve wind direction from sub-images containing WSs and spiral rain bands. For sub-images with WSs, wavelet transform is used to retrieve wind direction, while for sub-images with rain bands, edge detection methods are employed to locate the TC eye center and the tangent to the spiral rain band is then used to determine the wind direction associated with the rain band. This approach mitigates errors introduced by rain bands in SAR images, thereby enhancing the accuracy of wind direction inference. The retrieved results are compared with reanalysis data from the European Centre for Medium-Range Weather Forecasts (ECMWF) and wind direction data from the HRD observation productions to validate the effectiveness of the method. The organization of this paper is as follows: Section 2 provides a brief overview of the datasets used in the study. Section 3 details the sub-image recognition method based on transfer learning with the Inception V3 neural network and the wind direction retrieval techniques. Section 4 presents the wind direction retrieval and validation results for TCs Douglas and Larry, as well as the results for 10 TCs. Finally, Section 5 concludes the study.

2. Materials and Dataset

2.1. Sentinel-1 SAR Images

The Sentinel-1 mission is one of five missions launched by the European Space Agency (ESA) as part of the Copernicus Earth observation initiative. It consists of two C-band SAR satellites (Sentinel-1 A and Sentinel-1 B), equipped with C-band SAR sensors operating at a central frequency of 5.404 GHz. These satellites operate in four imaging modes: Strip-map (SM), Interferometric Wide Swath (IW), Extra Wide Swath (EW), and Wave (WV). Sentinel-1 can provide dual-polarization images (VV + VH), where backscattered signals are received in vertical and horizontal polarizations. Sentinel-1 is utilized to provide observational

data for research and development across various domains, such as terrestrial monitoring, atmospheric environment, ocean monitoring, and climate [25]. The Satellite Hurricane Observation Campaign (SHOC) is an initiative launched by the European Space Agency (ESA) following the peak of hurricane activity in 2016. Its objective is to collect observational data on hurricanes, primarily focusing on obtaining maximum Sentinel-1 products from within the hurricane eye or its periphery. These data are integrated with other sources to facilitate research into hurricane development and evolution. The Sentinel-1 mission serves as the primary means for SHOC to acquire essential resources. Therefore, SHOC is significant for accurately estimating TC parameters under extreme weather conditions using SAR in TC scenarios. This study utilizes TC SAR images from the SHOC period as research data, with all SAR images resampled.

This study utilizes the SAR image dataset established by Wang et al. [26], which comprises a subset of over 37,000 Sentinel-1 SAR images in WV mode over the ocean surface. This annotated dataset summarizes the geophysical properties and imaging characteristics of ten defined phenomena observed in spaceborne SAR images. It is applicable to scientific and engineering applications across various fields, such as deep learning, remote sensing, oceanography, and meteorology. Since the focus of this study is on TCs, we specifically selected WSs, rain bands, and other geophysical phenomena as our objects of study, as illustrated in Figure 1. The chosen features primarily include WSs and rain bands, while other geophysical phenomena in SAR images are classified as a third category.
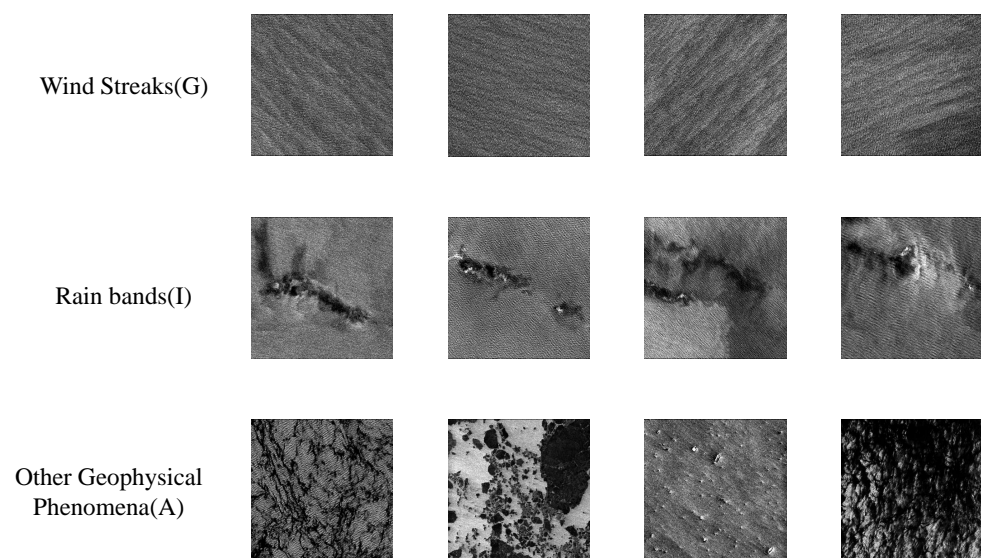
Figure 1. Example of geophysical phenomena in SAR images. The first row represents wind streaks (G), the second row depicts rain bands (I), and the third row illustrates other geophysical phenomena (A).

The Sentinel Application Platform (SNAP) provided by the ESA is used for preprocessing SAR images, including thermal noise removal, radiometric calibration, and speckle noise filtering. Land masking is applied to avoid attempting to estimate wind direction over land areas. The next step involves data calibration to achieve NRCS values that are independent of the incidence angle. The third processing step involves employing an enhanced Lee filter to suppress speckle noise, utilizing local statistical properties to smooth homogeneous regions while preserving edge information.

In this study, SAR image information from 10 Sentinel-1 images with well-defined TC eyes worldwide during the SHOC period from 2016 to 2021 was collected. Table 1 presents detailed information on the SAR images of TCs. This paper utilizes dual-polarization SAR images at Level-1 Ground Range Detected (L1GRD), with images in IW mode having a bandwidth of 250 km, an incidence angle range of 29° to 31°, and a pixel size of 10 m × 10 m.

This study employs dual-polarization SAR images for TCs wind direction retrieval, as the use of VH polarization images yields superior results [19]. Ni et al. [20] found that combining VH and VV polarization images for wind direction retrieval provides better outcomes compared to using single-polarization methods.

Table 1. TCs SAR images captured by Sentinel-1 for wind direction retrieval and validation.

TC Name	Acquisition Time	Satellite	Acquisition Mode	Polarization	Category	ATCF (V_{max} (m/s))	Ocean
Irma	7 September 2017 10:29:51	S1-A	IW	VV + VH	5	75	Atlantic
Maria	21 September 2017 22:46:26	S1-A	IW	VV + VH	3	56	Atlantic
Maria	23 September 2017 10:43:49	S1-B	IW	VV + VH	3	51	Atlantic
Hector	7 August 2018 15:45:02	S1-A	EW	VV + VH	4	59	Pacific
Michael	9 October 2018 23:43:05	S1-A	EW	VV + VH	3	56	Atlantic
Michael	10 October 2018 11:49:07	S1-A	EW	VV + VH	4	64	Atlantic
Dorian	30 August 2019 22:45:48	S1-A	IW	VV + VH	4	58	Atlantic
Douglas	25 July 2020 03:47:55	S1-A	EW	VV + VH	3	50	Pacific
Delta	8 October 2020 00:07:02	S1-B	IW	VV + VH	1	41	Atlantic
Larry	7 September 2021 21:46:30	S1-B	EW	VV + VH	3	51	Atlantic

2.2. HRD Observation Wind Products

The Hurricane Research Division (HRD) is a research department within the National Oceanic and Atmospheric Administration (NOAA). Each year, HRD conducts field observation missions on NOAA's research aircraft, focusing on the study of tropical cyclones and associated weather phenomena. During reconnaissance missions of tropical cyclones, the United States Air Force records flight level parameters, including wind direction, with a time resolution of 1 Hz [27]. This study utilizes HRD's TCs observational data to supplement the ECMWF reanalysis data and uses the processed and calculated wind direction at a height of 10 m above ground level as the reference wind direction for this research. This study utilizes a time window of 2 h, aligning SAR image acquisition time with HRD observation time to ensure accuracy.

2.3. ECMWF Reanalysis Products

This study employs the ERA5 reanalysis wind dataset from the European Centre for Medium-Range Weather Forecasts (ECMWF). This dataset, derived from the Integrated Forecasting System (IFS) of ECMWF, provides 10-m equivalent stress wind data and offers global wind field information dating back to 1979. It is widely utilized for research into atmospheric and oceanic processes. In this study, the ERA5 data are used for comparative analysis with wind directions retrieved from SAR observations. The dataset has spatial and temporal resolutions of 0.25° and 1 h, respectively [28]. It is important to note that the ERA5 reanalysis data need to be spatially shifted to align with the center of the TCs in the SAR images.

3. Methodology

The methods for retrieving sea surface wind direction from SAR images primarily include wavelet transform methods, LG, FFT, texture feature-based analysis, image pro-

cessing techniques, and deep learning approaches. However, the presence of significant rain bands around tropical cyclones (TCs) introduces substantial errors in wind direction retrieval. To address this issue, this study proposes a transfer learning-based Inception V3 neural network for identifying wind streaks (WSs) and rain bands in SAR images under TC conditions. Different methods are employed to retrieve wind direction from sub-images containing WSs and spiral rain bands. The overall workflow is illustrated in Figure 2.
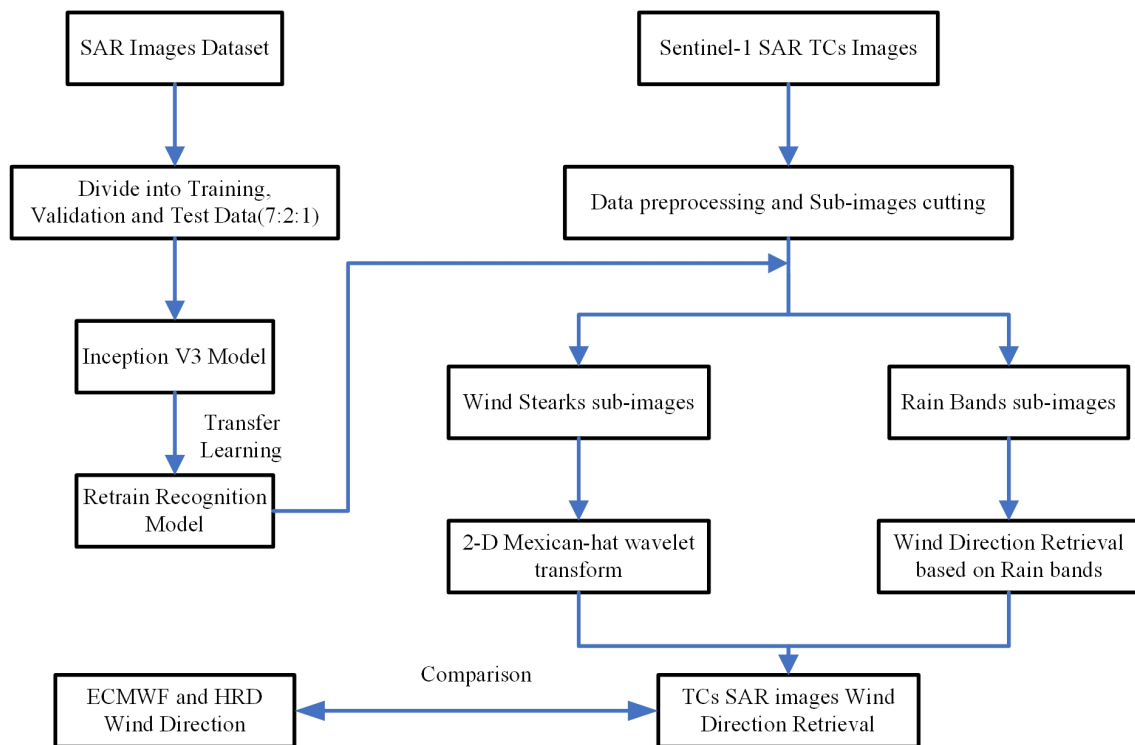
Figure 2. Flowchart of retrain recognition model based on transfer learning and wind direction retrieval from TCs SAR images.

3.1. The Inception V3 Convolutional Neural Network

This paper employs a Convolutional Neural Network (CNN) as the training model for identifying phenomena in TC SAR sub-images. The rationale for choosing a CNN lies in its capability as a deep learning model to automatically extract features from image data, thereby avoiding manual feature engineering. Through convolutional layers, CNNs achieve local perception, effectively recognizing local features within images. Parameter sharing reduces model complexity and the number of training parameters, thus enhancing training efficiency and generalization ability [29,30]. Additionally, CNNs excel in extracting features such as texture, color, and shape from images, providing significant advantages in image processing [31]. Inception Net is one of the typical models within CNNs, initially developed and used by Google in 2014 [32]. Based on deep CNNs architecture, it has been applied to tasks such as image classification and computer vision. The Inception Net includes various versions from V1 to V4. This paper utilizes the Inception V3 model. Inception V3 improves upon its predecessors by optimizing network structure and computational methods. It maintains accuracy while enhancing operational speed and computational efficiency. This model introduces multiple asymmetrically sized convolutional kernels and pooling layers, employing parallel operations to handle features of various scales simultaneously. This enhancement boosts the network's capability to recognize objects of different sizes, thereby demonstrating superior performance in image classification with higher accuracy rates.

Due to the depth of the Inception V3 network architecture reaching 48 layers and the complexity of training parameters, retraining the model poses significant challenges. To circumvent these difficulties, this paper employs transfer learning. Transfer learning is

a machine learning technique where a model developed for task A serves as the starting point and is reused or adapted for task B, as depicted in Figure 3. The primary method involves training a model on a large dataset to learn weights. During retraining, these weights are transferred to a new network for further training. In this study, we retain the convolutional and pooling layers of the pre-trained Inception V3 model to extract features from SAR images and fine-tune the model to recognize geophysical phenomena in these images. Notably, transfer learning is particularly useful when there is a lack of sample data, allowing effective utilization of smaller training image datasets [32].
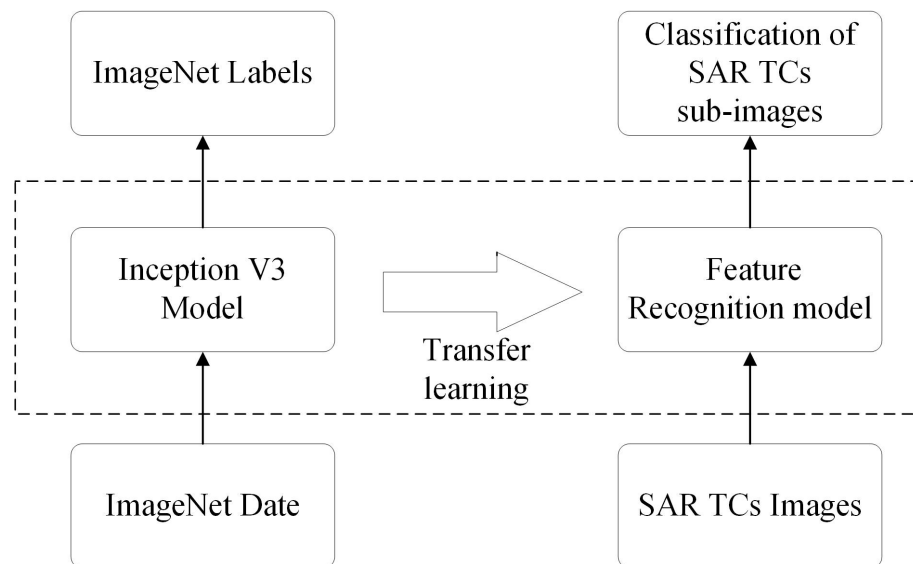
Figure 3. The architecture of transfer learning.

3.2. Edge Detection Algorithm

Edge detection technology is an image processing technique used to identify and locate edges or contours within an image. Edges typically represent regions where there are significant changes in brightness or color, which are often related to boundaries or shapes within the image. Due to the substantial gradient changes in the intensity of the dark rain band stripes in SAR images, edge detection operators can be employed to detect rain bands in SAR TC images [18]. TCs are powerful storm systems in the atmosphere, characterized by heavy precipitation. In SAR images, these areas of heavy precipitation often appear as spiral band structures extending from the center of the tropical cyclone outward. This study utilizes edge detection operators to compute the pixel intensity gradients near the rain band stripes in SAR images, thereby revealing spiral-like patterns. For this purpose, dual-polarization (VV + VH) SAR images are employed for the aforementioned edge detection. Common edge detection algorithms include the Sobel operator, Canny operator, Prewitt edge detection algorithm, and wavelet-based edge detection methods. However, the Canny operator, which employs a double-threshold technique to detect and connect edge points, provides more accurate detection of rain band stripes. Therefore, this study uses the Canny operator. Additionally, the Canny operator applies the first derivative of a two-dimensional Gaussian function for image smoothing, calculates the magnitude and direction of the gray scale gradient using a first-order differential operator, and performs non-maximum suppression, thereby enhancing the clarity of rain band stripes in SAR images.

The gradient intensities in the horizontal and vertical directions of the first-order differential operator are computed using G_x and G_y, respectively

$$G_x = \begin{bmatrix} -1 & 0 & +1 \\ -2 & 0 & +2 \\ -1 & 0 & +1 \end{bmatrix} \quad \text{and} \quad G_y = \begin{bmatrix} +1 & +2 & +1 \\ 0 & 0 & 0 \\ -1 & -2 & -1 \end{bmatrix} \tag{1}$$

$$G = \sqrt{G_x^2 + G_y^2} \tag{2}$$

$$\theta = \tan^{-1}\left(\frac{G_x}{G_y}\right) \tag{3}$$

where G represents the magnitude of the gradient and θ denotes the direction of the gradient.

3.3. Wind Direction Retrieval

In this study, we initially utilized the SNAP for the preprocessing of SAR images, which includes thermal noise removal, orbital correction, GRD boundary noise removal, speckle noise filtering, and terrain correction. After preprocessing, we performed resampling on the EW and IW mode SAR images, resulting in a final SAR image resolution of 40 m × 40 m. Subsequently, we divided the SAR images into sub-images of size 250 × 250 pixels, with each sub-image having an actual size of approximately 10 km × 10 km, to facilitate the use of deep learning methods for identifying whether a sub-image contains WSs or rain bands.

Wavelet analysis is a mathematical method that finds applications across various fields, including signal processing, image processing, computer classification and recognition, medical imaging and diagnosis, as well as engineering fault diagnosis [33]. When wavelet transform is employed for SAR image processing, it enables multi-scale decomposition of SAR images, allowing for the characterization of wind direction information at different spatial scales. Consequently, the striped information in SAR images can be utilized to retrieve wind direction. The wavelet transform method is based on the two-dimensional (2-D) Fourier transform, which transfers the image from the spatial domain to the frequency domain. Two frequency components can be clearly identified through two pairs of maxima [14] . For each sub-image containing WSs, the 2-D wavelet transform method is employed to retrieve wind direction. Wavelet analysis provides both time-domain and frequency-domain localization capabilities and can automatically adjust the time-frequency window to meet actual analysis needs.

Assume $f(t)$ and $\psi(t)$ are square-integrable functions, both belonging to the space of square-integrable functions. Then, the continuous wavelet transform of the signal $f(t)$ is given by

$$W_f(a,b) = \int_R f(t) \cdot \bar{\psi}_{ab}(t)\, dt \tag{4}$$

where $\psi_{ab}(t)$ represents the wavelet basis, which results from translating and scaling the mother wavelet $\psi(t)$. The wavelet basis is expressed as

$$\psi_{ab}(t) = |a|^{1/2} \psi\left(\frac{t-b}{a}\right) \tag{5}$$

where a and b are the scale and translation parameters, respectively, representing the frequency and time parameters in $\psi_{ab}(t)$. Among the common wavelet mother functions, the Mexican-hat wavelet is known for its excellent local capabilities in both the time and frequency domains, making it particularly useful for extracting WSs information from SAR images. The 2-D Mexican-hat wavelet transform is represented as

$$\psi_h(\boldsymbol{k}) = (\boldsymbol{k} \cdot \boldsymbol{k}) \exp\left(\frac{1}{2(\boldsymbol{k} \cdot \boldsymbol{k})}\right) \tag{6}$$

where $\boldsymbol{k}$ represents the variables in the 2-D space-frequency domain. The wavenumber spectrum of the WSs in the SAR images is then computed using the 2-D FFT transform method

$$S_{m,n} = \sum_{a=1}^{N} \sum_{b=1}^{N} G_{a,b} \exp\left(-2\pi i \cdot \frac{m \cdot a + n \cdot b}{N}\right) \tag{7}$$

where $S_{m,n}$ represents the wavenumber spectrum of the WSs in the SAR images, and G denotes the grayscale values of the SAR images, with $m, n \in \mathbb{N}_+$. By drawing vertical lines

through the peaks of the 2-D wavenumber spectrum, the sea surface wind direction can be retrieved.

For each sub-image containing wind streaks, we use the Canny edge detection operator to perform feature detection on the rain bands in the TCs SAR images.

In this study, more than three clear rain bands from each SAR image for both polarization modes were selected, and this paper utilizes the arcuate distribution pattern of rain band streaks around the TCs center to calculate the geographical location of the TC's eye. Selecting more than three rain band streaks aims to reduce errors from the random distribution of rain bands. Additionally, results from both polarization modes are combined to determine the TC's eye position, and the spiral pattern of rain bands around the TC's eye is utilized to establish the wind direction at this location. The procedure for determining wind direction is as follows:

(1) Utilize the Canny edge detector to identify rain band streaks in SAR images with VV and VH polarization.
(2) Select more than three clear rain band streaks with an arcuate distribution.
(3) Using the characteristic of the arcuate rain band streaks spiraling towards the TC's eye, this study defines the perpendicular bisector of the spiral rain band, deviating inward by 20°, as the center of the spiral rain band and the TC's eye. The tangent to the spiral rain band at this point represents the wind direction.
(4) Compute the average position of the TC's eye from multiple spiral calculations in VV and VH polarizations as the final result.
(5) Determine the wind direction based on the tangent direction of the spiral centered at the TC's eye.

In this study, the wind direction is taken as 20° inward deviation from the tangent direction of the rain band to the TC eye position, as illustrated in Figure 4.
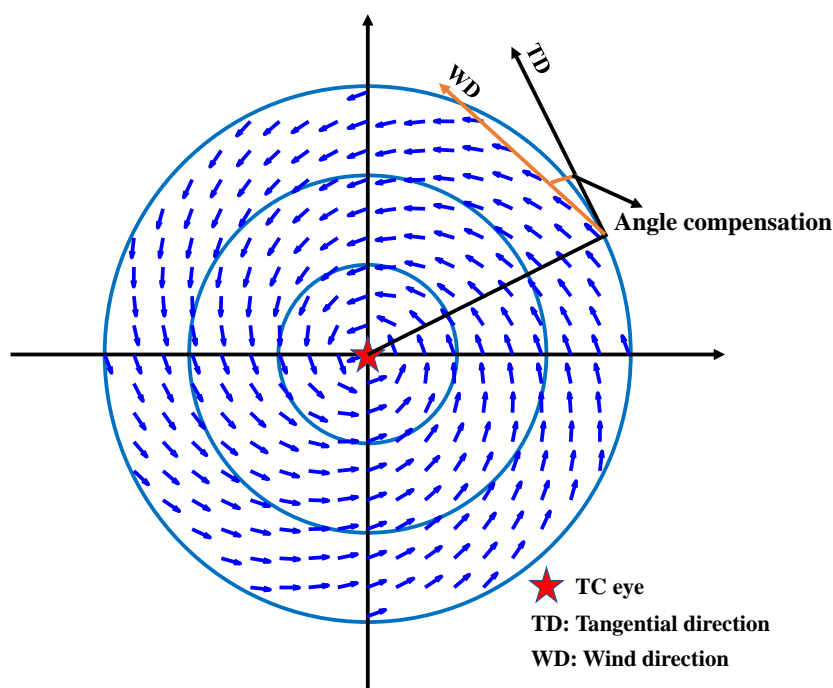
Figure 4. The wind direction of rain band locations existing in Northern Hemisphere TCs.
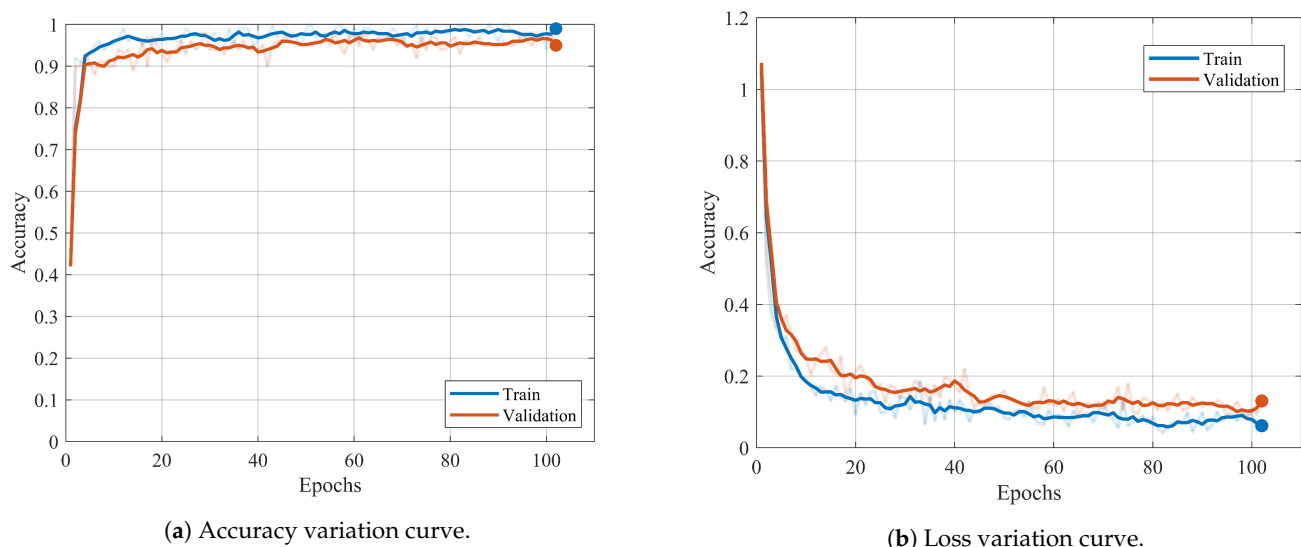
4. Results and Validation

4.1. Recognition of SAR Sub-Images

This paper employs transfer learning-based deep learning methods for SAR sub-image recognition. Initially, suitable feature datasets for TCs were selected from the atmospheric ocean phenomenon dataset [26]. The deep learning dataset comprises 4797 SAR sub-images

with WSs, 4740 SAR sub-images with rain bands, and 5000 SAR sub-images with other geophysical phenomena. This dataset is divided into three subsets: training, validation, and test data, with a ratio of 7:2:1. Figure 5 shows the retraining and validation results based on the transfer learning model. Figure 5a depicts the accuracy curves for the training and validation sets over epochs, while Figure 5b shows the loss curves over thes epochs. The results indicate that the accuracy for both the training and validation sets increases rapidly at the beginning of the epochs, while the loss decreases quickly until stabilizing around the 40th epoch. The accuracy of the training set is slightly higher than that of the validation set.

From the variation in accuracy and loss, it can be observed that the accuracy of the validation set starts below 50% and eventually reaches 97.5%, while the loss decreases from greater than 1 to 0.0907. This preliminary analysis suggests that the transfer learning-based Inception V3 model is capable of identifying WSs and rain bands in SAR images. Consequently, we proceeded to use this model to recognize rain bands and WSs in SAR images containing TCs and employed different methods to retrieve wind direction based on the recognition results.

(**a**) Accuracy variation curve.

(**b**) Loss variation curve.

**Figure 5.** Accuracy and loss of training set (blue lines) and validation set (orange lines).

In this study, SAR images under TC conditions are segmented into 10 km × 10 km sub-images. The sub-images are then identified using a transfer learning-based Inception V3 convolutional neural network. Figure 6a presents the sub-image identification results for SAR images of TC Douglas captured by Sentinel-1 on 25 July 2020, while Figure 6b shows the sub-image identification results for TC Larry on 7 September 2021.

4.2. Wavelet Transform-Based Wind Direction Retrieval for SAR WSs Sub-Images

In this study, a wind direction retrieval method based on wavelet analysis is employed for SAR sub-images identified by the model as WSs geophysical phenomena. Accordingly, sub-images labeled as G are input into a 2-D Mexico-hat wavelet transform model to determine their wind direction. Figure 7 presents the results of wind direction retrieval for a sub-image using this method. Specifically, Figure 7a shows the preprocessed SAR sub-image. Figure 7b,c display the results after FFT transformation and Mexico-hat wavelet transformation, respectively. In Figure 7d, the red solid line indicates the direction of the power spectrum variation, while the white dashed line denotes the wind direction.

(**a**) Case TC Douglas.

(**b**) Case TC Larry.
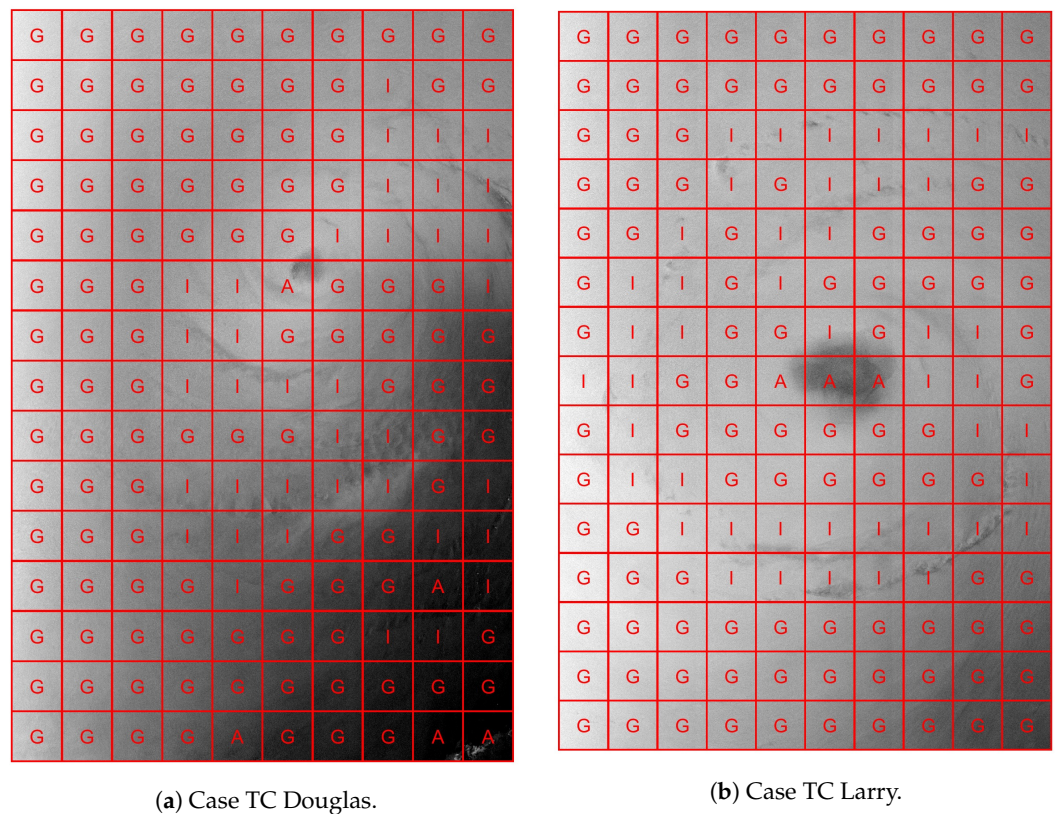
Figure 6. Sub-image recognition results of SAR TC images. "G" represents WSs, "I" represents rain bands and "A" denotes other geophysical phenomena.
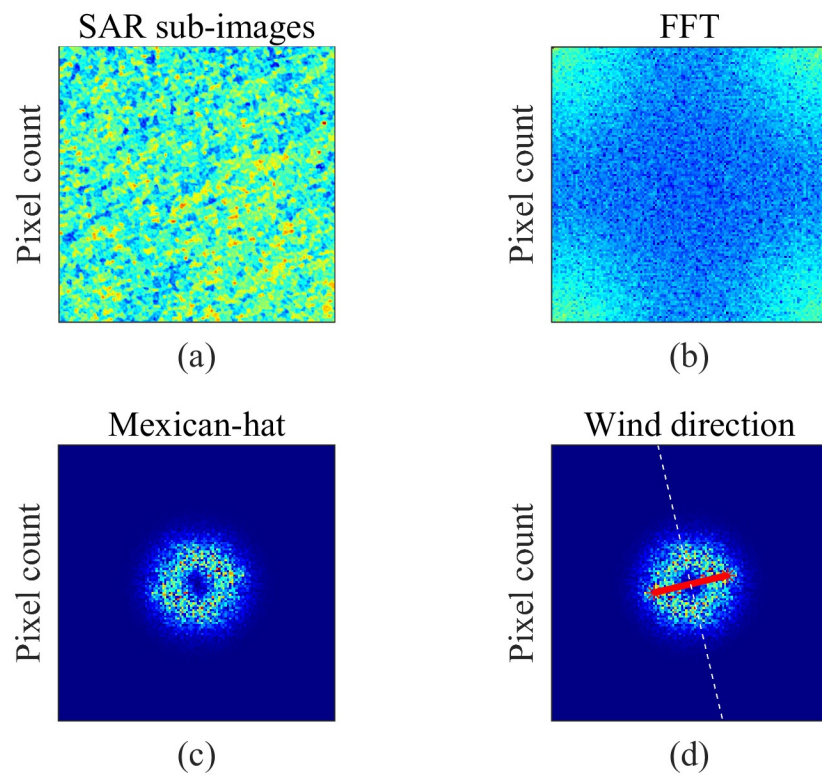
Figure 7. Wind direction retrieval from SAR TC sub-images using 2-D Mexican-hat wavelet transform. (**a**) SAR sub-image; (**b**) The result of FFT; (**c**) The result of Mexico-hat wavelet transformation; (**d**) The wind direction of the sub-image.

4.3. Wind Direction Retrieval Method for SAR Rain Bands Sub-Images

In this study, edge detection methods from image processing are employed to identify rain bands in SAR images, where WSs appear as dark, stripe-like features. The Canny edge detector is used due to its capability to set two thresholds, which enhances the detection of WSs. Figure 8 presents the results of edge detection for rain bands in the SAR image of TC Douglas. Processing SAR images is conducted in both VV and VH polarization modes. Figure 8b,e show rain band stripes obtained under VV and VH polarizations, respectively. The thresholds of the Canny operator were (0.054, 0.056) for VV polarization and (0.010, 0.013) for VH polarization. It was observed that edge detection methods are more effective for detecting rain bands in VV-polarized SAR images, whereas VH polarization is more susceptible to strip noise and wind sensitivity, which can impact detection results. The rain band stripes were selected, and the average position of the TC eye was determined, as shown in Figure 8c,f, where the rain band stripes are indicated within the boxes and the TC eye position is marked by red dots. Figure 9 illustrates the corresponding results for TC Larry, which were acquired on 7 September 2021. The thresholds of the Canny operator for TC Larry were (0.008, 0.020) for VV polarization and (0.230, 0.250) for VH polarization.
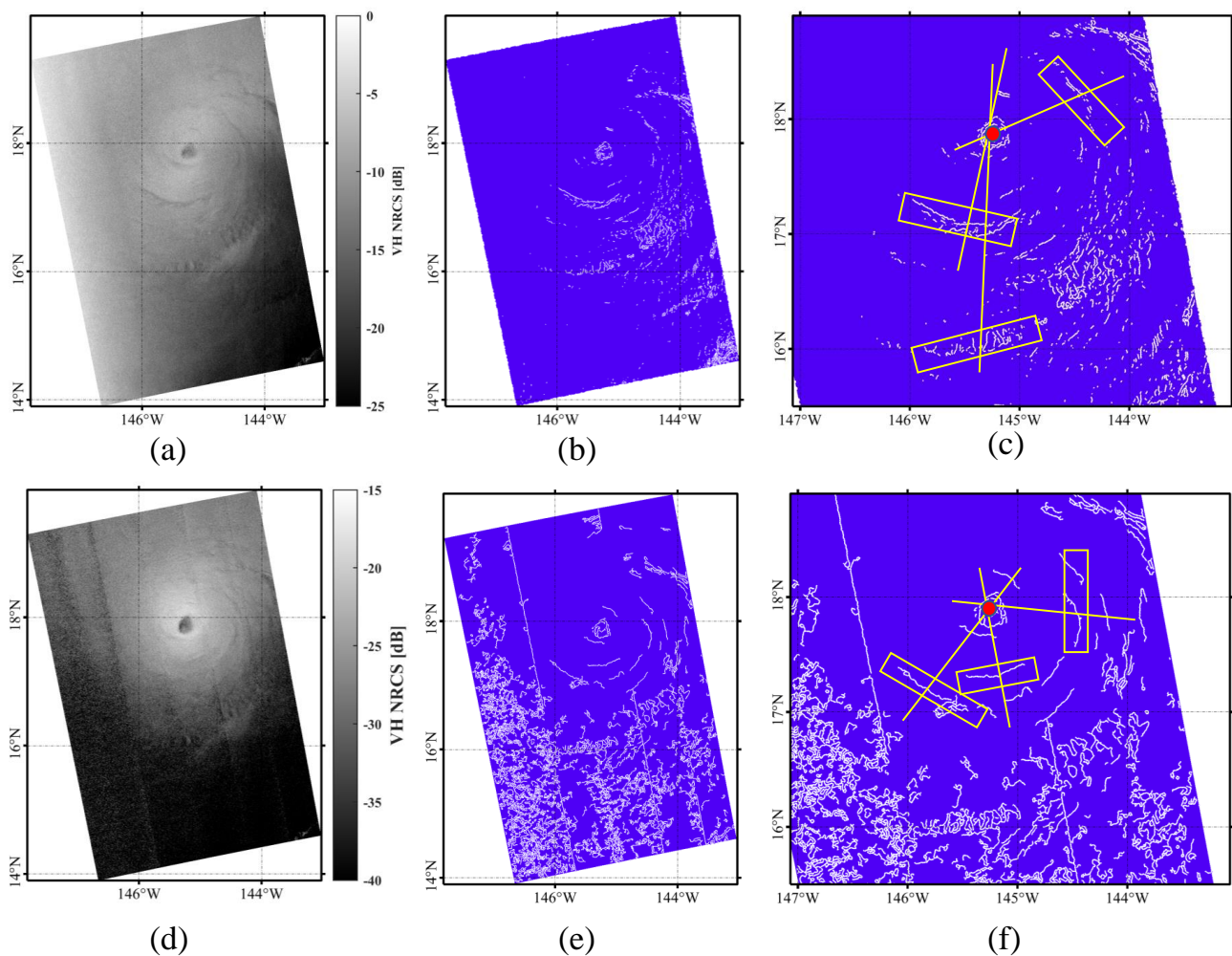
Figure 8. The Canny edge detection results for TC Douglas. The NRCS for VV and VH polarizations are presented in (**a**,**d**), respectively; the rain band distributions for VV and VH polarizations are shown in (**b**,**e**), respectively; the TC eye positions for VV and VH polarizations are depicted in (**c**,**f**), respectively.
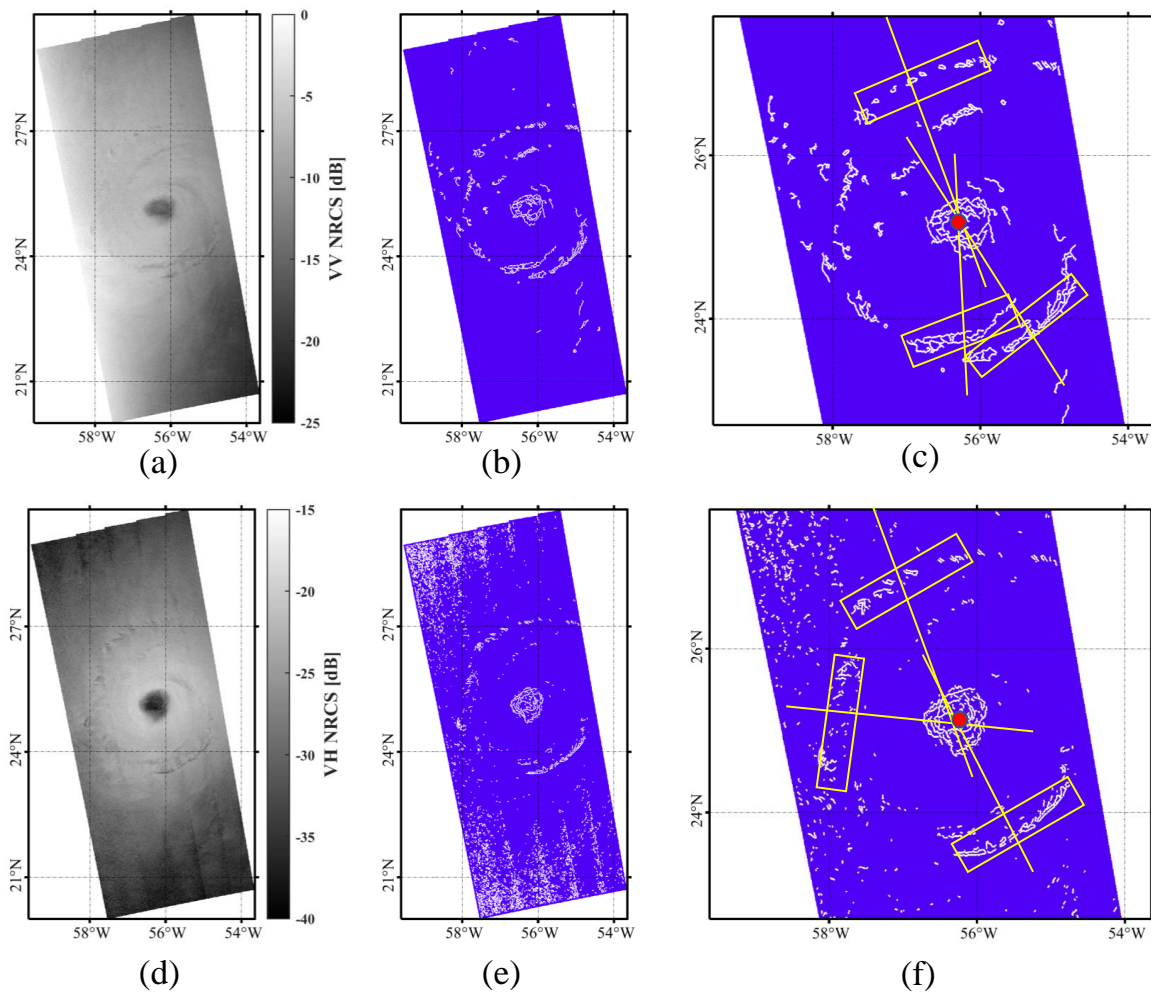
Figure 9. The Canny edge detection results for TC Larry. The NRCS for VV and VH polarizations are presented in (**a**,**d**), respectively; the rain band distributions for VV and VH polarizations are shown in (**b**,**e**), respectively; the TC eye positions for VV and VH polarizations are depicted in (**c**,**f**), respectively.

4.4. Wind Direction Ambiguity Removal and Results Validation

When performing wind direction retrieval from SAR images, the issue of 180° wind direction ambiguity is typically encountered. Therefore, it is necessary to resolve this ambiguity in the wind direction retrieval results. In general sea area, the wind ambiguity removal method often relies on external data. However, for tropical cyclones, due to their unique rotational patterns, it is possible to resolve the ambiguity without external wind direction information. This uncertainty can be addressed by utilizing the distinct rotational modes of tropical cyclones in the Northern and Southern Hemispheres. For each sub-image's wind direction, there are two possibilities (resulting in 180° ambiguity), represented in the diagram as $\theta_{p_{i1}}$ and $\theta_{p_{i2}}$, as shown in Figure 10. The process of removing wind direction ambiguity in this study consists of the following steps:

(1) Determine the TC's eye position using an edge detection algorithm.
(2) Account for the TC's rotational direction: counterclockwise in the Northern Hemisphere and clockwise in the Southern Hemisphere.
(3) Taking the Northern Hemisphere as an example, the distribution of the counterclockwise rotating wind field is illustrated in Figure 4, serving as a rough reference for the

counterclockwise wind direction; note that in the Southern Hemisphere, the rotation is clockwise.

(4) Determine the position of the sub-image in relation to the center of the tropical cyclone.

(5) Select the wind direction solution that is closest to the estimate provided in (3) as the final result: As shown in Figure 10, the retrieved wind direction of the sub-image (with a 180° ambiguity) is denoted as θ_p, and the reference wind direction value is denoted as θ_t and $\Delta\theta = |\theta_{p_i} - \theta_t|$, when $\Delta\theta$ is minimized, θ_{p_i} represents the de-ambiguous wind direction.

Figure 11a illustrates the rotational pattern of TCs in the Northern Hemisphere, while Figure 11b shows the rotational pattern in the Southern Hemisphere. Note that in this study, wind direction is defined as 0° for north.

By employing the aforementioned wind direction de-ambiguation method, combined with wavelet analysis for SAR sub-images exhibiting WSs and edge detection for SAR sub-images with rain bands, the wind direction of TCs from SAR images was retrieved. Additionally, nonlinear interpolation was used to estimate wind direction for SAR sub-images identified as other geophysical phenomena, enabling retrieval of the wind direction of TCs throughout the entire SAR image.

Figure 12b illustrates the wind direction retrieval results for TC Douglas, with the black arrows indicating the retrieved wind direction, and Figure 12c presents the corresponding wind direction from ECMWF, demonstrating satisfactory consistency between the SAR retrieval results and the reference wind estimates. Figure 12d shows a scatter plot of the wind direction retrieval results from SAR images against the ECMWF and HRD observation wind direction, with a correlation coefficient of 0.96, a bias of 2.15°, and the RMSD is 20.80°.
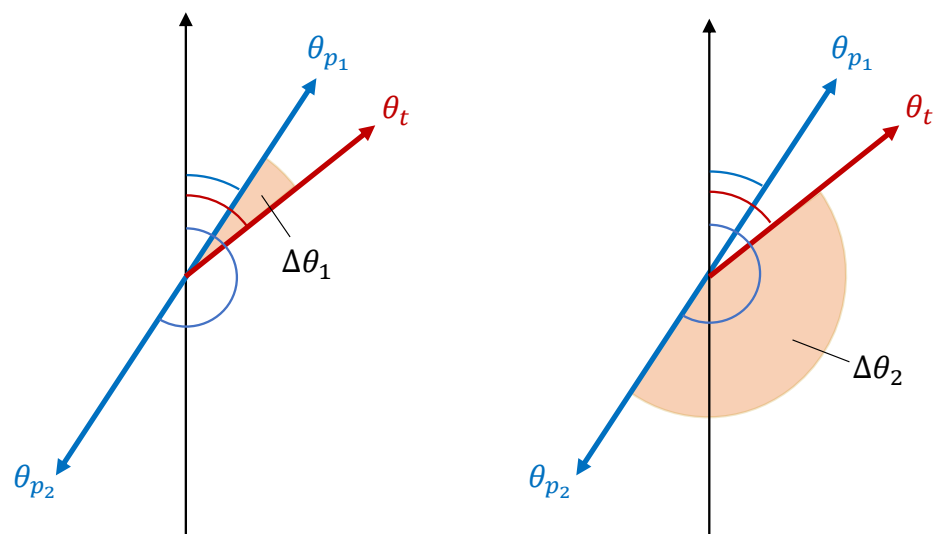

Figure 10. Schematic diagram of wind directions with 180° ambiguity and reference wind direction. For the two predicted wind directions θ_{p_1} and θ_{p_2} that are aligned but point in opposite directions, the smaller the $\Delta\theta$ calculated relative to the reference wind direction θ_t, the closer it is to the true wind direction.

Figure 13 displays the sea surface wind direction retrieved of TC Larry. Specifically, Figure 13d presents a scatter plot comparing the retrieved wind direction from SAR with the estimated direction from the configured wind reference, yielding a correlation coefficient of 0.96, a bias of 0.47°, and the RMSD is 19.66°. These results indicate a strong agreement between the SAR retrieved wind direction and the ECMWF and HRD observation wind direction, demonstrating the feasibility and robustness of the proposed method.
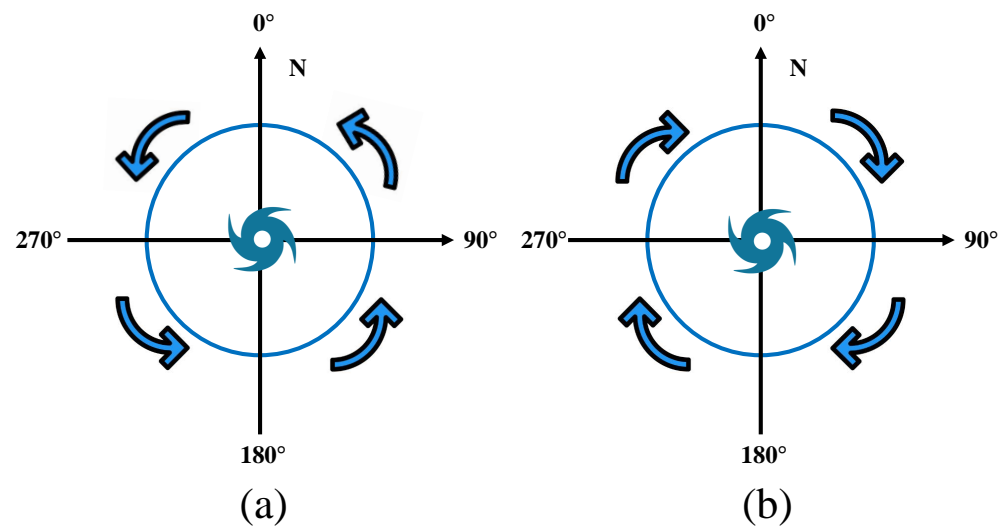
Figure 11. The wind field rotational pattern of TCs. (**a**) TCs in the Northern Hemisphere. (**b**) TCs in the Southern Hemisphere.
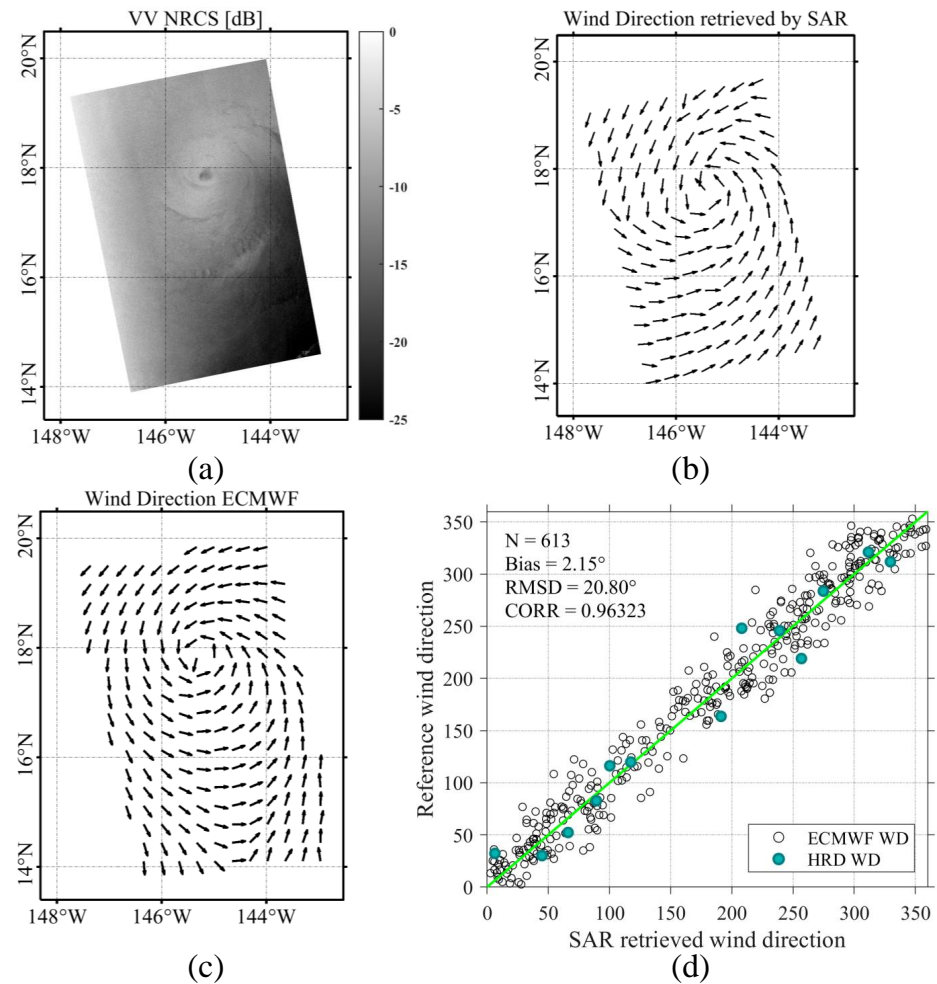

Figure 12. The wind direction retrieval results for TC Douglas, acquired on 25 July 2020. (**a**) Quick-look from the VV polarized SAR image over TC Douglas; (**b**) The wind direction retrieval results; (**c**) The ECMWF wind direction; (**d**) Comparison of the retrieved wind direction with ECMWF and HRD observation wind direction.
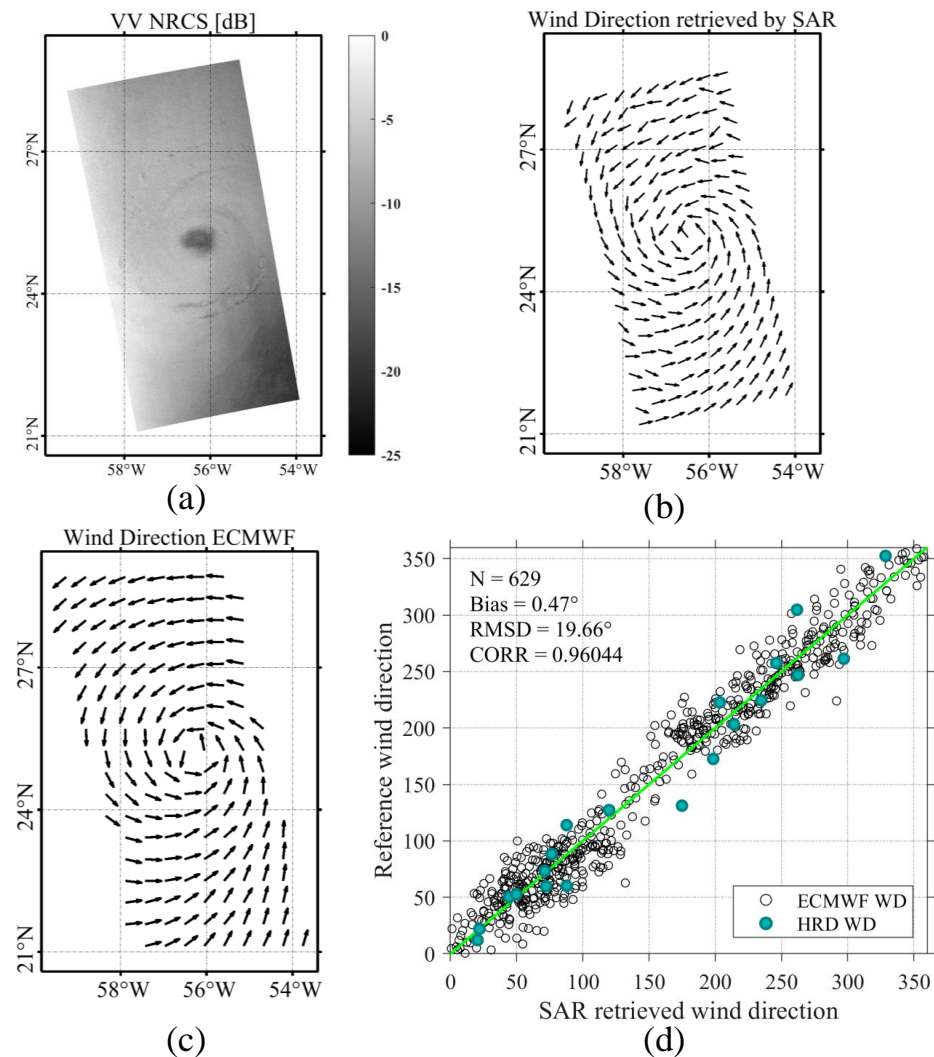
Figure 13. The wind direction retrieval results for TC Larry, acquired on 7 September 2021. (**a**) Quick-look from the VV polarized SAR image over TC Larry; (**b**) The wind direction retrieval results; (**c**) The ECMWF wind direction; (**d**) Comparison of the retrieved wind direction with ECMWF and HRD observation wind direction.

Beyond the individual case studies mentioned earlier, this paper extends the validation of the proposed method to all SAR images containing TCs listed in Table 1. Since ECMWF wind field forecast data provide global coverage, they were used as the reference for validating the wind direction retrieval results. A statistical comparison was conducted between the wind directions retrieved from SAR images and the ECMWF wind direction data, as illustrated in Figure 14. A total of 7723 comparisons were made. The results show that the wind direction retrievals from SAR images under most TC conditions are consistent with the ECMWF and HRD reference wind direction, with a bias of 0.31°, and RMSD is 19.52°, and a correlation coefficient of 0.96.

However, some retrieval results differed by more than 20°, which is attributed to the higher smoothness of the ECMWF reanalysis data, causing discrepancies in a small number of wind direction retrievals. Despite these discrepancies, the overall statistical results indicate that the wind direction retrieval accuracy from SAR images of TCs using the proposed method is high, thus validating the reliability of this technique.
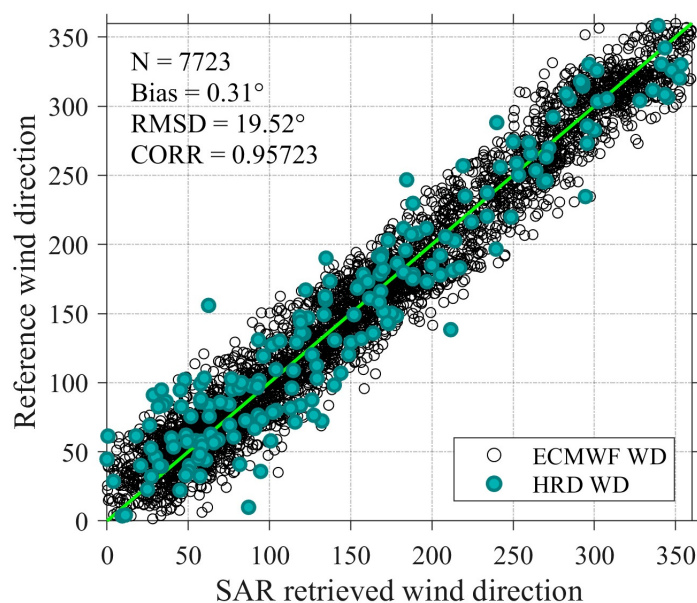
Figure 14. Comparison of wind directions retrieved from 10 SAR TCs images with ECMWF reanalysis and HRD observation wind directions.

In addition, Table 2 summarizes the performance of traditional FFT and LG methods used for SAR wind direction retrieval in published studies. The method employed in this paper is referred to as the "WSs and RBs method" to emphasize its implementation of wind direction retrieval based on wind streaks and rain bands, respectively, while summarizing its performance. Furthermore, due to the differences in the SAR TC data and wind field reference values used in various methods, these discrepancies inevitably affect the accuracy of each approach, therefore this study conducted only a relative comparison.

Table 2. Summary of the performance of FFT and LG wind direction methods and the performance of this study.

Source	Method	Reference Wind Direction	RMSD
Zhou et al. 2017 [34]	FFT	ECMWF CCMP *	30.22° 25.41°
	LG	ECMWF CCMP	36.10° 36.65°
Zheng et al. 2018 [35]	FFT	ECMWF CCMP	23.00° 23.43°
	LG	ECMWF CCMP	30.96° 30.43°
This Study	WSs and RBs method	ECMWF and HRD	19.52°

* Cross-Calibrated Multi-Platform (CCMP) wind vector product.

5. Discussion

TCs are often accompanied by extreme weather events, such as strong winds and heavy rainfall, which have significant impacts and hazards for human activities. The wind field of TCs exhibits considerable variability, making accurate retrieval of the wind field crucial for TC monitoring. Traditional TC monitoring methods, which rely on ground-based meteorological observations, have notable limitations, while remote sensing has emerged as a means for large-scale observation of the ocean surface. SAR, with its high resolution, provides more detailed information for TC observation. Additionally, during the SHOC

period, a wealth of TC SAR images was acquired, providing valuable data for the study of extreme wind fields at the sea surface.

In recent decades, research on retrieving wind fields from SAR images has been continuously advancing. Currently, the calculation of sea surface wind speed relies on geophysical model functions (GMFs), most of which require wind direction as a priori information. Therefore, retrieving wind direction is critical for constructing the wind vector field of TCs. This paper proposes a novel method for retrieving the wind direction of TCs from Sentinel-1 SAR images by classifying sub-images within TC conditions. The approach utilizes 10 SAR images acquired under TC conditions. Firstly, SAR images are classified using the Inception V3 model based on transfer learning, distinguishing between sub-images with WSs and those with rain bands. After accurately identifying the WSs in the SAR sub-images, wind direction retrieval is performed using the Mexican-hat wavelet transform method. For sub-images containing rain bands, the vortex model is applied to retrieve the wind direction, which is then aggregated to obtain the wind direction for the TC SAR images. Case studies of TCs Douglas and Larry demonstrate that the proposed method achieves RMSD of 20.80° and 19.66°, compared to ECMWF reanalysis and HRD observation wind direction, validating the accuracy of the retrieved wind direction. Additionally, a quantitative validation across a total of 10 TCs indicates that this method consistently provides the most accurate TC wind directions. The statistical results indicate an RMSD of 19.52°, and a correlation coefficient of 0.96. These results affirm the potential application of the proposed method for TC wind direction retrieval. Several factors can be considered to improve accuracy in wind direction retrieval. Notably, significant precipitation creates distinct rain bands in TC SAR images; the wind direction retrieval from sub-images containing these rain bands relies on their detection. However, heavy rainfall can lead to signal attenuation in SAR images, potentially introducing errors in wind direction retrieval. Future research should address the impact of precipitation on NRCS attenuation as a crucial factor in wind field retrieval. Additionally, the rapid changes in wind direction near the TC eye can contribute to errors in the final results. These factors should be considered in future work to further enhance the accuracy of TC wind direction retrieval from SAR images.

References

1. Huang, L.; Li, X.; Liu, B.; Zhang, J.A.; Shen, D.; Zhang, Z.; Yu, W. Tropical cyclone boundary layer rolls in synthetic aperture radar imagery. *J. Geophys. Res. Ocean.* **2018**, *123*, 2981–2996. [CrossRef]
2. Jin, S.; Li, X.; Yang, X.; Zhang, J.A.; Shen, D. Identification of tropical cyclone centers in SAR imagery based on template matching and particle swarm optimization algorithms. *IEEE Trans. Geosci. Remote Sens.* **2018**, *57*, 598–608. [CrossRef]
3. Zhang, G.; Perrie, W.; Zhang, B.; Yang, J.; He, Y. Monitoring of tropical cyclone structures in ten years of RADARSAT-2 SAR images. *Remote Sens. Environ.* **2020**, *236*, 111449. [CrossRef]
4. Pierson, W.J., Jr. The measurement of the synoptic scale wind over the ocean. *J. Geophys. Res. Ocean.* **1983**, *88*, 1683–1708. [CrossRef]
5. Gerling, T. Structure of the surface wind field from the Seasat SAR. *J. Geophys. Res. Ocean.* **1986**, *91*, 2308–2320. [CrossRef]
6. Hersbach, H. Comparison of C-band scatterometer CMOD5. N equivalent neutral winds with ECMWF. *J. Atmos. Ocean. Technol.* **2010**, *27*, 721–736. [CrossRef]
7. Quilfen, Y.; Bentamy, A. Calibration/validation of ERS-1 scatterometer precision products. In Proceedings of the IGARSS'94-1994 IEEE International Geoscience and Remote Sensing Symposium, Pasadena, CA, USA, 8–12 August 1994; Volume 2, pp. 945–947.
8. Horstmann, J.; Koch, W. Ocean wind field retrieval using ENVISAT ASAR data. In Proceedings of the IGARSS 2003. 2003 IEEE International Geoscience and Remote Sensing Symposium. Proceedings (IEEE Cat. No. 03CH37477), Toulouse, France, 21–25 July 2003; Volume 5, pp. 3102–3104.
9. Shao, W.; Zhou, Y.; Zhang, Q.; Jiang, X. Machine Learning-Based Wind Direction Retrieval From Quad-Polarized Gaofen-3 SAR Images. *IEEE J. Sel. Top. Appl. Earth Obs. Remote Sens.* **2023**, *17*, 808–816. [CrossRef]
10. Furevik, B.R.; Johannessen, O.M.; Sandvik, A.D. SAR-retrieved wind in polar regions-comparison with in situ data and atmospheric model output. *IEEE Trans. Geosci. Remote Sens.* **2002**, *40*, 1720–1732. [CrossRef]
11. Lehner, S.; Horstmann, J.; Koch, W.; Rosenthal, W. Mesoscale wind measurements using recalibrated ERS SAR images. *J. Geophys. Res. Ocean.* **1998**, *103*, 7847–7856. [CrossRef]
12. Zhang, R.; Yan, W.; Ai, W.; Ma, S. A Method of Ocean Surface Wind Direction Retrievals for Airborne SAR Images Based on Gabor Wavelet Transform. *J. Microw.* **2011**, *27*, 79–83. [CrossRef]
13. Zecchetto, S. Wind direction extraction from SAR in coastal areas. *Remote Sens.* **2018**, *10*, 261. [CrossRef]
14. Corazza, A.; Khenchaf, A.; Comblet, F. Assessment of Wind Direction Estimation Methods from SAR Images. *Remote Sens.* **2020**, *12*, 3631. [CrossRef]
15. Koch, W. Directional analysis of SAR images aiming at wind direction. *IEEE Trans. Geosci. Remote Sens.* **2004**, *42*, 702–710. [CrossRef]
16. Zhu, H.; Wen, B.; Huang, J. Wind Directions Retrieval Based on Scale Partitioned SAR Images' Gradients. *J. Wuhan Univ. Sci. Ed.* **2005**, *51*, 375–378.
17. Rana, F.M.; Adamo, M.; Pasquariello, G.; De Carolis, G.; Morelli, S. LG-Mod: A Modified Local Gradient (LG) Method to Retrieve SAR Sea Surface Wind Directions in Marine Coastal Areas. *J. Sens.* **2016**, *2016*, 9565208. [CrossRef]
18. Xie, T.; Geng, X.; Edwing, K.; Liu, D.; Jian, C.; Yan, X.H. Tropical cyclone wind direction retrieval from sentinel-1 SAR imagery by a modified Improved Local Gradient (ILG-Mod) method. *Remote Sens. Lett.* **2023**, *14*, 1335–1346. [CrossRef]
19. Fan, S.; Zhang, B.; Mouche, A. Tropical Cyclone Wind Direction Retrieval from C-Band Dual-Polarization Synthetic Aperture Radar. In Proceedings of the 2018 Progress in Electromagnetics Research Symposium (PIERS-Toyama), Toyama, Japan, 1–4 August 2018; pp. 1423–1427.
20. Ni, W.; Stoffelen, A.; Ren, K. Tropical cyclone wind direction retrieval from dual-polarized SAR imagery using histogram of oriented gradients and Hann window function. *IEEE J. Sel. Top. Appl. Earth Obs. Remote Sens.* **2022**, *16*, 878–888. [CrossRef]
21. Du, Y.; Vachon, P.W.; Wolfe, J. Wind direction estimation from SAR images of the ocean using wavelet analysis. *Can. J. Remote Sens.* **2002**, *28*, 498–509. [CrossRef]
22. Wang, Y.; Zheng, G.; Zhou, L.; Qiu, Z.; Li, X.; Zhou, Y. Wind direction retrieval of tropical cyclone from SAR imagery using improved local gradient method. In Proceedings of the IOP Conference Series: Earth and Environmental Science, Chengdu, China, 18–20 July 2020; IOP Publishing: Bristol, UK, 2020; Volume 569, p. 012055.
23. Gao, Y.; Guan, C.; Sun, J.; Xie, L. A New Hurricane Wind Direction Retrieval Method for SAR Images without Hurricane Eye. *J. Atmos. Ocean. Technol.* **2018**, *35*, 2229–2239. [CrossRef]
24. Guo, C.; Ai, W.; Hu, S.; Du, X.; Chen, N. Sea surface wind direction retrieval based on convolution neural network and wavelet analysis. *IEEE J. Sel. Top. Appl. Earth Obs. Remote Sens.* **2022**, *15*, 3868–3876. [CrossRef]
25. Geudtner, D.; Torres, R.; Snoeij, P.; Bibby, D.; Rommen, B. Sentinel-1 system. In Proceedings of the EUSAR 2014; 10th European Conference on Synthetic Aperture Radar, Berlin, Germany, 3–5 June 2014; pp. 1–3.
26. Wang, C.; Mouche, A.; Tandeo, P.; Stopa, J.E.; Longépé, N.; Erhard, G.; Foster, R.C.; Vandemark, D.; Chapron, B. A labelled ocean SAR imagery dataset of ten geophysical phenomena from Sentinel-1 wave mode. *Geosci. Data J.* **2019**, *6*, 105–115. [CrossRef]
27. Powell, M.D.; Black, P.G. The relationship of hurricane reconnaissance flight-level wind measurements to winds measured by NOAA's oceanic platforms. *J. Wind. Eng. Ind. Aerodyn.* **1990**, *36*, 381–392. [CrossRef]
28. Yao, J.; Miao, Y.; Kumara, P.T.P.; Arulananthan, K.; Zhang, Z.; Zhou, W. Analysis of Wind Energy Potential in Sri Lankan Waters Based on ERA5 (ECMWF Reanalysis v5) and CCMP (Cross-Calibrated Multi-Platform). *J. Mar. Sci. Eng.* **2024**, *12*, 876. [CrossRef]

29. Li, Z.; Liu, F.; Yang, W.; Peng, S.; Zhou, J. A survey of convolutional neural networks: Analysis, applications, and prospects. *IEEE Trans. Neural Netw. Learn. Syst.* **2021**, *33*, 6999–7019. [CrossRef] [PubMed]

30. Indolia, S.; Goswami, A.K.; Mishra, S.P.; Asopa, P. Conceptual understanding of convolutional neural network-a deep learning approach. *Procedia Comput. Sci.* **2018**, *132*, 679–688. [CrossRef]

31. Guo, C.; Ai, W.; Zhang, X.; Guan, Y.; Liu, Y.; Hu, S.; Zhao, X. Correction of sea surface wind speed based on SAR rainfall grade classification using convolutional neural network. *IEEE J. Sel. Top. Appl. Earth Obs. Remote Sens.* **2022**, *16*, 321–328. [CrossRef]

32. Alom, M.Z.; Taha, T.M.; Yakopcic, C.; Westberg, S.; Sidike, P.; Nasrin, M.S.; Van Esesn, B.C.; Awwal, A.A.S.; Asari, V.K. The history began from alexnet: A comprehensive survey on deep learning approaches. *arXiv* **2018**, arXiv:1803.01164.

33. Lei, Z.; Hanqing, S.; Huadong, D.; Xian, C.; Hailong, D. Estimation of sea surface wind direction using spaceborne SAR images and wavelet analysis. *J. Remote Sens.* **2014**, *18*, 215–230. [CrossRef]

34. Zhou, L.; Zheng, G.; Li, X.; Yang, J.; Ren, L.; Chen, P.; Zhang, H.; Lou, X. An Improved Local Gradient Method for Sea Surface Wind Direction Retrieval from SAR Imagery. *Remote Sens.* **2017**, *9*, 671. [CrossRef]

35. Zheng, G.; Li, X.; Zhou, L.; Yang, J.; Ren, L.; Chen, P.; Zhang, H.; Lou, X. Development of a Gray-Level Co-Occurrence Matrix-Based Texture Orientation Estimation Method and Its Application in Sea Surface Wind Direction Retrieval from SAR Imagery. *IEEE Trans. Geosci. Remote Sens.* **2018**, *56*, 5244–5260. [CrossRef]